



## Constructing Hierarchical Porous Zeolites via Kinetic Regulation

Kunlun Ding,<sup>†,||</sup> Avelino Corma,<sup>‡</sup> Juan Antonio Maciá-Agulló,<sup>‡</sup> Jerry G. Hu,<sup>§</sup> Stephan Krämer,<sup>§</sup> Peter C. Stair,<sup>||</sup> and Galen D. Stucky<sup>\*,†</sup>

<sup>†</sup>Department of Chemistry and Biochemistry, University of California, Santa Barbara, California 93106, United States

<sup>‡</sup>Instituto de Tecnología Química, Universidad Politécnica de Valencia-Consejo Superior de Investigaciones Científicas (UPV-CSIC), Av. de los Naranjos s/n, 46022 Valencia, Spain

<sup>§</sup>Materials Research Laboratory, University of California, Santa Barbara, California 93106, United States

<sup>||</sup>Department of Chemistry, Northwestern University, Evanston, Illinois 60208, United States

### **S Supporting Information**

**ABSTRACT:** Zeolites are crystalline inorganic solids with microporous structures, having widespread applications in the fields of catalysis, separation, adsorption, microelectronics, and medical diagnosis. A major drawback of zeolites is the mass transfer limitation due to the small size of the micropores (less than 1 nm). Numerous efforts have been dedicated to integrating mesopores with the microporous zeolite structures by using templating and/or destructive approaches. Here we provide a new strategy for hierarchical pore size zeolite synthesis, without using supramolecular or hard templates. The branching epitaxial growth behavior, as a result of aluminum-zoning, contributes to the formation of the hierarchical porous zeolite structures.

Zeolites have been widely used as catalysts in many industrial processes, such as fluid catalytic cracking (FCC), isomerization, alkylation, methanol-to-gasoline/methanol-to-olefin, etc.<sup>1–4</sup> Reactant and product diffusion limitations, which are inherited from the microporous nature of the zeolite structures, can substantially restrict the zeolite catalytic performance. In many cases only the very thin outer layer of a zeolite crystal contributes to the catalytic activity, while the inner part of the zeolite crystal stays silent during the catalysis because the interior sites are less accessible.<sup>5</sup> The situation becomes even more challenging for bulky molecule reactions, for instance, waste polymer (polyethylene, polypropylene, etc.) cracking and biomass conversions.<sup>6</sup> Introducing mesopores into the microporous zeolite structures is able to solve the aforementioned problem. Mesopores give zeolites a new dimension that shortens the overall required micropore diffusion length.<sup>7</sup> Therefore, faster diffusion and more accessible active sites are made available. Moreover by facilitating product diffusion and transport, mesopores make the zeolite catalysts less susceptible to deactivations, such as coking.<sup>8</sup>

Several approaches have been developed to construct hierarchical porous zeolites that contain both mesopores and micropores, including destructive approaches such as demetallation<sup>9</sup> and recrystallization;<sup>10,11</sup> and constructive approaches such as using hard templates,<sup>12–14</sup> supramolecular templates,<sup>8,15–17</sup> and surface silanization.<sup>18</sup> Despite these elegant achievements, a cost-effective mesoporous zeolite synthesis is still yet to be

developed.<sup>19</sup> Constructing hierarchical porous zeolite solely by regulating the kinetics of zeolite nucleation and growth has long been a dream because of its simplicity and potential industrial viability.

A recent breakthrough<sup>20</sup> showed that using tetrabutyl structure-directing agents (SDAs), instead of tetrapropyl ammonium (the most common SDA for MFI-type zeolite synthesis), led to the formation of a house-of-cards structure, composed of repetitively branched ultrathin nanosheets. It was postulated that tetrabutyl SDAs, unlike their tetrapropyl analogues, were not well accommodated within the MFI framework and inhibited MFI crystal growth along the *b*-axis. Therefore, the formation of single unit cell lamellae is favored.

Here we report a new synthetic strategy for constructing hierarchical porous MFI-type zeolites simply by regulating the nucleation and growth kinetics. The most common SDA, tetrapropyl ammonium, was employed in our synthesis. No supramolecular or hard template is needed. Aluminum-zoning was found to be the reason for the branching epitaxial growth of the MFI zeolite crystals.

We were interested in employing a two-step crystallization process in hierarchical porous zeolite synthesis based on the following hypothesis. During the first step, which should be performed at low temperatures (20–80 °C), most precursors hydrolyze and condense to form precrystallized clusters; these clusters aggregate in an oriented-attachment manner at medium temperatures (100–140 °C) during the second step of synthesis. The avoidance of Ostwald ripening at lower temperatures allows the retaining of defects generated in the oriented-attachment process. Detailed synthesis protocols are described in the *Supporting Information*. In practice, a mixture of  $n_{\text{TPAOH}}/n_{\text{Al}}/n_{\text{Si}}/n_{\text{H}_2\text{O}}$  (Al denotes Al(sec-BuO)<sub>3</sub>, Si denotes TEOS) was first aged at low temperature ( $T_1$ ) for a certain period ( $t_1$ ); and the resulting clear solution was then heated up to higher temperature ( $T_2 = 120$  °C) for another period ( $t_2$ ) to give the zeolite product denoted as  $n_{\text{TPAOH}}/n_{\text{Al}}/n_{\text{Si}}/n_{\text{H}_2\text{O}} - T_1(t_1) - T_2(t_2)$ . All the zeolites reported in this work are MFI structures, as confirmed by X-ray diffraction analyses (Figure S1, *Supporting Information*). A typical yield of zeolite product is ca. 70%.

**Received:** June 30, 2015

**Published:** August 31, 2015



Figure 1 shows two typical zeolite morphologies, which resulted from different TPAOH concentrations. 3/0.2/10/

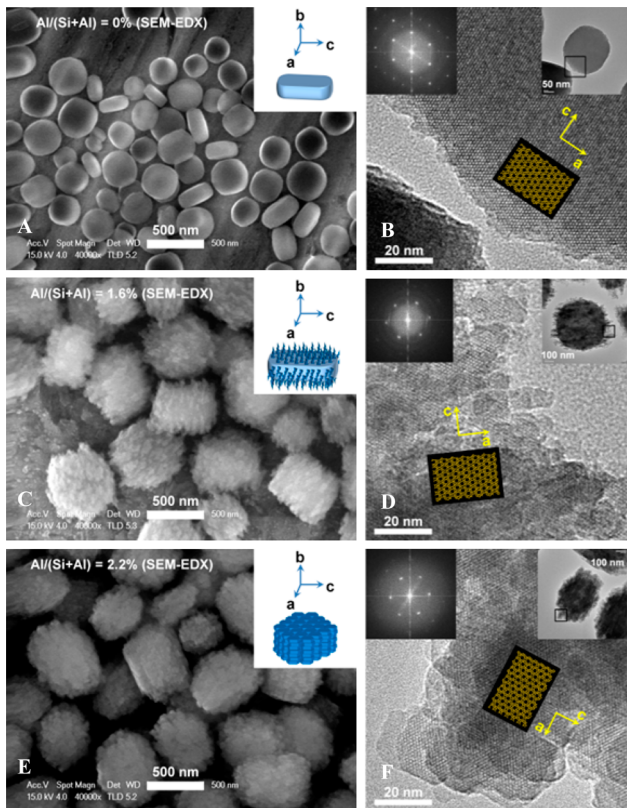


**Figure 1.** SEM and TEM images of the zeolites 3/0.2/10/1000–20 °C(2d)–120 °C(4h) (A,B), 3/0.2/10/1000–20 °C(2d)–120 °C(1d) (C,D), and 5/0.2/10/1000–20 °C(2d)–120 °C(1d) (E,F). The insets of (A), (C), and (E) show the simulated crystal shapes and orientations. The high-resolution TEM images were taken from the marked area of their insets. Fast Fourier transform (FFT) of (B), (D), and (F) are shown in their insets.

1000–20 °C(2d)–120 °C(1d) gives a core–shell morphology, which is composed of a nonmesoporous core and an epitaxially grown hyperbranched shell. The epitaxial growth is evidenced by high-resolution transmission electron microscopy (TEM) analyses, which show that all the branches have identical crystal orientations, thus confirming their single-crystalline nature (Figures 1D and S2). Scanning electron microscopy (SEM) and TEM images show that the 100 nm-thick shell is full of mesopores and macropores. Nitrogen adsorption–desorption analyses show that the size of these mesopores and macropores ranges from 10 to 100 nm, as shown in Figure S3, which is consistent with our SEM and TEM observations. 5/0.2/10/1000–20 °C(2d)–120 °C(1d) also gives a core–shell morphology, except that the shell is composed of nanoplates instead of branches. Similar to the product described above, these nanoplates have identical crystal orientations (Figures 1E,F and S4). Compared to irregular branches, nanoplates tend to densely pack, resulting in fewer mesopores. Indeed, N<sub>2</sub> sorption analysis shows that the mesopore surface area and mesopore volume of the nanoplate-composed zeolite are smaller than those of the branched zeolite (Table S1).

In order to explore the formation mechanism of these hierarchical porous zeolite structures, we isolated the short reaction time products by centrifugation. As seen in Figures 1A,B

and S5, 3/0.2/10/1000–20 °C(2d)–120 °C(4h) and 5/0.2/10/1000–20 °C(2d)–120 °C(4h) give similar product morphologies. Plate-shape zeolite nanocrystals with smooth surfaces are formed in both cases. The normal of the plate-like zeolite nanocrystal is along the *b*-axis of the MFI structure. Energy dispersive X-ray (EDX) analyses of these short reaction time (4 h) products show negligible Al content. In contrast, the long reaction time (24 h) products contain a significant amount of Al, as evidenced by inductively coupled plasma atomic emission spectroscopy (ICP-AES), SEM-EDX, and nuclear magnetic resonance (NMR) studies (Figures 2C and S6). These results

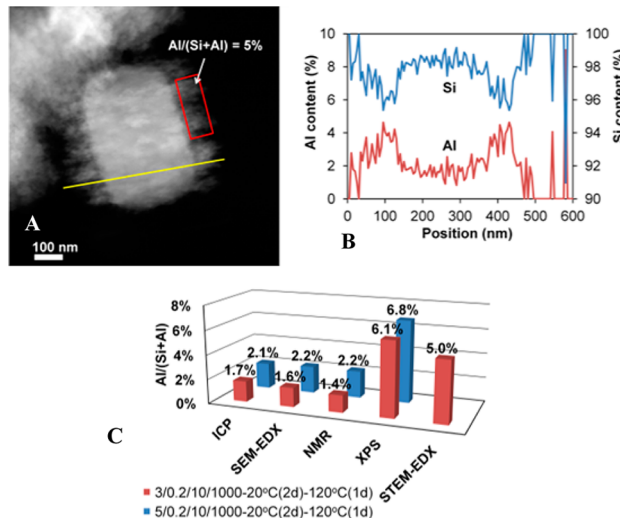


**Figure 2.** (A) HAADF-STEM image of the zeolite 3/0.2/10/1000–20 °C(2d)–120 °C(1d). (B) Line-scan EDX results along the line shown in (A). (C) Aluminum contents of the zeolites 3/0.2/10/1000–20 °C(2d)–120 °C(1d) and 5/0.2/10/1000–20 °C(2d)–120 °C(1d) based on different techniques.

suggest that most of the Al should be enriched in the rim of the zeolite crystals. X-ray photoelectron spectroscopy (XPS) is known as a surface analysis technique, which also confirms the Al enrichment in the surface layers (Figure 2C). In order to further verify the Al-zoning, we carried out more detailed EDX analysis on 3/0.2/10/1000–20 °C(2d)–120 °C(1d) zeolite crystals under high-angle annular dark-field scanning transmission electron microscopy (HAADF-STEM) mode, with the results shown in Figure 2A,B. An EDX line-scan across the zeolite crystal clearly shows the enrichment of Al along the rim structure. A selected area EDX shows that the rim of the zeolite crystal contains about 5% Al (relative to Si), which is about three times the average Al content of 1.6%.

The Al-zoning in ZSM-5 (MFI structure) has been reported in several studies.<sup>21–25</sup> Groen et al.<sup>23</sup> showed that a controlled desilication of the Al-zoned ZSM-5 crystals could etch out the Si-rich cores, forming hollow particles with a well-preserved Al-rich exterior. Weckhuysen et al.<sup>25</sup> used synchrotron-based micro-meter-resolved XRD to map the lattice parameters along the zeolite ZSM-5 crystal. Since the lattice parameters can be correlated with the incorporation of Al in the tetrahedral positions of a pure silica parent framework, they were able to crystallographically map the differences in concentration of Al within a single crystal. As they pointed out, the crystal lattice expands because of the longer average Al–O distance (1.75 Å) compared to the Si–O distance (1.61 Å).<sup>25</sup> Here we believe that under our synthetic conditions, the Al-induced distortion of the

crystal structure leads to the formation of crystallographic defects, which account for the branching growth behavior of the zeolites. This type of growth behavior has not been observed to date since most zeolite syntheses have been carried out at higher temperatures (150–180 °C) as opposed to 120 °C in our synthesis. The crystallographic defects can be easily cured at elevated temperatures in a hydrothermal environment.

In order to verify our hypothesis that Al is the key to the branching growth behavior, we varied the Si/Al ratio in the starting solution of the synthesis. Figure S7 shows that smooth zeolite crystals with similar sizes were formed if there was no Al or a very small amount of Al in the solution (Si/Al ratio of 200/1). These Al-deficient solutions turned translucent in 1.5 h at 120 °C, while the solution with more Al (Si/Al ratio of 50/1) stayed transparent and clear until 4 h at 120 °C. This suggests that the crystallization kinetics slowed upon the introduction of Al, which may originate from the structure distortion by Al. A stronger kinetic-inhibition effect was observed when we tried to extend our synthesis protocol to the Ga-MFI system, as the Ga–O distance (~1.9 Å)<sup>26</sup> is greater than the Al–O distance (1.75 Å). Aging and crystallization of Ga/Si system in a one-pot manner did not give any solid product at 120 °C in 1 day. Alternatively, when a Ga-free solution and a Ga/Si solution were aged separately and mixed immediately before the crystallization stage at 120 °C, Ga-MFI zeolites were obtained in less than 1 day (Figure S8).

We studied next how these branches were formed. Instead of isolating the large zeolite crystals by centrifugation, we analyzed the crude solution of 3/0.2/10/1000–20 °C(2d)–120 °C(4h) and 3/0.2/10/1000–20 °C(2d)–120 °C(1d) using TEM. Aside from the smooth zeolite crystals in the size range of 200–300 nm, many amorphous nanoparticles with sizes <10 nm were observed (Figure S9). The existence and the size of these nanoparticles were confirmed by dynamic light scattering (DLS) measurement (Figure S10). Similar-sized nanoparticles were also observed in the crude solution of 3/0.2/10/1000–20 °C(2d)–120 °C(1d), except that these nanoparticles became more crystalline (Figure S11). Oriented-attachment of these nanoparticles to the bigger zeolite crystals was observed (Figure S11).

The above observations suggest that the formation of these hierarchical zeolite structures follows a multistep mechanism, which is illustrated in Figure 3. The first step is the low-

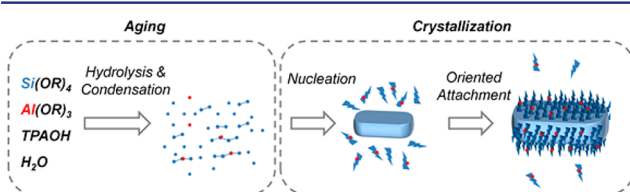


**Figure 3.** Mechanistic illustration of the hierarchical porous zeolite structure formation.

temperature aging of the precursor solution. In this step, molecular precursors hydrolyze and condense to form silicate and aluminosilicate polyanions.<sup>27,28</sup> The second step is the early stage of the high-temperature crystallization process, where silicate polyanions nucleate and grow into Al-free MFI zeolite crystals; and meanwhile, the aluminosilicate polyanions slowly crystallize into Al-rich MFI zeolite nanocrystals. The final step is the oriented-attachment of the Al-rich MFI nanocrystals onto the Al-free MFI crystals to give the Al-zoned hierarchical zeolite

structures. This mechanism is in general agreement with our working hypothesis.

Our proposed branching mechanism is different than that proposed by Zhang et al. in their self-pillared pentasil zeolite synthesis.<sup>20</sup> They suggested that the MEL/MFI intergrowths might be the reason for the branching growth behavior, which eventually led to the house-of-cards zeolite structure with multiple twins. In our case, the oriented-attachment is clearly the reason for branching, which gives single-crystalline zeolite structures.

The morphology difference between 3/0.2/10/1000–20 °C(2d)–120 °C(1d) and 5/0.2/10/1000–20 °C(2d)–120 °C(1d) might be caused by the different pH of the solutions, as a different amount of TPAOH was added. Higher pH should facilitate the Ostwald ripening, which eliminates the crystallographic defects. Therefore, a more crystalline platelet structure is formed instead of the less crystalline branched structure. The pH effect is verified by lowering the amount of water while keeping all the other parameters identical. 3/0.2/10/600–20 °C(2d)–120 °C(1d) gives a zeolite morphology similar to that of 5/0.2/10/1000–20 °C(2d)–120 °C(1d) (Figure S12). As shown in Figure 4, further lowering the TPAOH/Si ratio from 3/10 to 2/

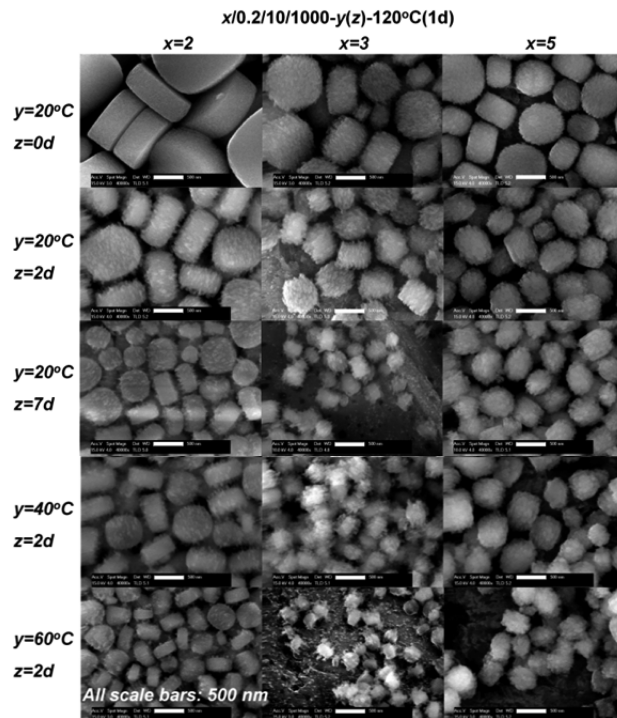


**Figure 4.** SEM images of the zeolite products synthesized with different TPAOH/Si ratios, aging times, and aging temperatures.

10 leads to significantly bigger zeolite crystals with similar morphologies, likely due to the decreased number of nuclei formed in solutions with lower pH.

In concert with the pH effect, increasing the crystallization temperature also accelerates the Ostwald ripening. The crude solution of 3/0.2/10/1000–20 °C(2d)–120 °C(1d) was further treated at 150 °C for 1 day, and the irregularly branched structure evolved into a more regular-shaped structure with larger crystalline domain size (Figure S13).

We next studied the low-temperature aging effect by varying the aging time and temperature of  $x/0.2/10/1000-y(z)-120^{\circ}\text{C}(1\text{d})$ . As described above, the precursors hydrolyze and

condense into polyanions during the aging process.<sup>27,28</sup> The aging time and temperature should have significant influence on the formation of the polyanions and consequently determine the morphology of the final zeolite product. As shown in Figure 4, increasing the aging time or the aging temperature leads to the formation of smaller zeolite crystals, which still possess core–shell structures (Figures S14 and S15). Such aging effects can be attributed to the increased structural ordering of the polyanions,<sup>29</sup> which not only shortens the nucleation period of the zeolite crystallization process but also increases the number of nuclei.<sup>30</sup>

We tested the catalytic performance of our hierarchical porous zeolite on the cracking of vacuum gas oil, wherein ZSM-5 is used as an additive to the main cracking zeolite, USY. The results are given in Figure S16. Compared to the commercial ZSM-5 sample, 5/0.2/10/1000–20 °C(2d)–120 °C(1d) gives slightly higher gas–oil cracking activity and similar gasoline yield, with more light cycle oil and slightly less coke formation. Furthermore, it gives less hydrogen transfer and therefore a higher olefin-to-paraffin ratio. From an industrial point of view, it is highly desired to increase the olefin-to-paraffin ratios, without too much penalty in gasoline.<sup>31</sup> Considering that USY plays a determining role in the catalytic cracking performance, the improvement caused by our HZSM-5 sample is evident. It seems that the hierarchical porous structure and the Al-zoning distribution have a positive effect on accessibility and avoidance of consecutive reactions.

In summary, we have demonstrated a new pathway for the construction of hierarchical porous zeolites. Single-crystalline core–shell MFI crystals with tunable sizes were obtained by regulating the zeolite nucleation and growth kinetics. Al-zoning was found to be the key to the branching epitaxial growth behavior, which resulted in the formation of a hierarchical porous shell. Most of the Al-related acid sites are located within the shell structure and, therefore, are highly accessible. The Si/Al gradient together with the hierarchical porous structure shows benefits in catalytic applications, such as FCC. Our results indicate that there is still more to learn about the mechanism of even the simplest zeolite synthesis. A greater in-depth understanding of zeolite nucleation and growth mechanisms would substantially benefit the design and synthesis of advanced zeolite structures.

## ■ ASSOCIATED CONTENT

### S Supporting Information

The Supporting Information is available free of charge on the ACS Publications website at DOI: [10.1021/jacs.5b06791](https://doi.org/10.1021/jacs.5b06791).

Experimental section, characterizations, Figures S1–S16, and Table S1 ([PDF](#))

## ■ AUTHOR INFORMATION

### Corresponding Author

\*[stucky@chem.ucsb.edu](mailto:stucky@chem.ucsb.edu)

### Notes

The authors declare no competing financial interest.

## ■ ACKNOWLEDGMENTS

This research was supported by the University of California Discovery Grant Program GCP08-128649 (to K.D. and G.D.S.) and the U.S. National Science Foundation CHE-1058835 (to K.D. and P.C.S.). A.C. thanks the program Severo Ochoa for financial support. J.A.M.-A. acknowledges the assistance of the CSIC for the award of a Postdoctoral JAE-Doc contract. This

research made extensive usage of the Shared Experimental Facilities of the Materials Research Laboratory, which are supported by the MRSEC Program of the NSF under Award No. DMR 1121053; a member of the NSF-funded Materials Research Facilities Network ([www.mrfn.org](http://www.mrfn.org)).

## ■ REFERENCES

- (1) Davis, M. E. *Nature* **2002**, *417*, 813.
- (2) Vermeiren, W.; Gilson, J. P. *Top. Catal.* **2009**, *52*, 1131.
- (3) Cejka, J.; Corma, A.; Zones, S. I. *Zeolites and Catalysis: Synthesis, Reactions and Applications*; Wiley-VCH: Weinheim, Germany, 2010.
- (4) Martinez, C.; Corma, A. *Coord. Chem. Rev.* **2011**, *255*, 1558.
- (5) Perez-Ramirez, J.; Christensen, C. H.; Egeblad, K.; Christensen, C. H.; Groen, J. C. *Chem. Soc. Rev.* **2008**, *37*, 2530.
- (6) Serrano, D. P.; Aguado, J.; Escola, J. M. *ACS Catal.* **2012**, *2*, 1924.
- (7) Moller, K.; Bein, T. *Chem. Soc. Rev.* **2013**, *42*, 3689.
- (8) Choi, M.; Na, K.; Kim, J.; Sakamoto, Y.; Terasaki, O.; Ryoo, R. *Nature* **2009**, *461*, 246.
- (9) Valtchev, V.; Majano, G.; Mintova, S.; Perez-Ramirez, J. *Chem. Soc. Rev.* **2013**, *42*, 263.
- (10) Moller, K.; Yilmaz, B.; Jacobinas, R. M.; Muller, U.; Bein, T. *J. Am. Chem. Soc.* **2011**, *133*, 5284.
- (11) Ivanova, I. I.; Knyazeva, E. E. *Chem. Soc. Rev.* **2013**, *42*, 3671.
- (12) Jacobsen, C. J. H.; Madsen, C.; Houzvicka, J.; Schmidt, I.; Carlsson, A. *J. Am. Chem. Soc.* **2000**, *122*, 7116.
- (13) Tao, Y. S.; Kanoh, H.; Kaneko, K. *J. Am. Chem. Soc.* **2003**, *125*, 6044.
- (14) Fan, W.; Snyder, M. A.; Kumar, S.; Lee, P. S.; Yoo, W. C.; McCormick, A. V.; Penn, R. L.; Stein, A.; Tsapatsis, M. *Nat. Mater.* **2008**, *7*, 984.
- (15) Liu, Y.; Zhang, W. Z.; Pinnavaia, T. J. *J. Am. Chem. Soc.* **2000**, *122*, 8791.
- (16) Na, K.; Jo, C.; Kim, J.; Cho, K.; Jung, J.; Seo, Y.; Messinger, R. J.; Chmelka, B. F.; Ryoo, R. *Science* **2011**, *333*, 328.
- (17) Liu, F. J.; Willhammar, T.; Wang, L.; Zhu, L. F.; Sun, Q.; Meng, X. J.; Carrillo-Cabrera, W.; Zou, X. D.; Xiao, F. S. *J. Am. Chem. Soc.* **2012**, *134*, 4557.
- (18) Choi, M.; Cho, H. S.; Srivastava, R.; Venkatesan, C.; Choi, D. H.; Ryoo, R. *Nat. Mater.* **2006**, *5*, 718.
- (19) Chal, R.; Gerardin, C.; Bulut, M.; van Donk, S. *ChemCatChem* **2011**, *3*, 67.
- (20) Zhang, X. Y.; Liu, D. X.; Xu, D. D.; Asahina, S.; Cychosz, K. A.; Agrawal, K. V.; Al Wahedi, Y.; Bhan, A.; Al Hashimi, S.; Terasaki, O.; Thommes, M.; Tsapatsis, M. *Science* **2012**, *336*, 1684.
- (21) Vonballmoos, R.; Meier, W. M. *Nature* **1981**, *289*, 782.
- (22) Althoff, R.; Schulzdoebrick, B.; Schuth, F.; Unger, K. *Microporous Mater.* **1993**, *1*, 207.
- (23) Groen, J. C.; Bach, T.; Ziese, U.; Donk, A. M. P. V.; de Jong, K. P.; Moulijn, J. A.; Perez-Ramirez, J. *J. Am. Chem. Soc.* **2005**, *127*, 10792.
- (24) Danilina, N.; Krumeich, F.; Castelanelli, S. A.; van Bokhoven, J. A. *J. Phys. Chem. C* **2010**, *114*, 6640.
- (25) Ristanovic, Z.; Hofmann, J. P.; Deka, U.; Schulli, T. U.; Rohrke, M.; Beale, A. M.; Weckhuysen, B. M. *Angew. Chem., Int. Ed.* **2013**, *52*, 13382.
- (26) Fricke, R.; Kosslick, H.; Lischke, G.; Richter, M. *Chem. Rev.* **2000**, *100*, 2303.
- (27) Cundy, C. S.; Cox, P. A. *Chem. Rev.* **2003**, *103*, 663.
- (28) Cundy, C. S.; Cox, P. A. *Microporous Mesoporous Mater.* **2005**, *82*, 1.
- (29) Davis, T. M.; Drews, T. O.; Ramanan, H.; He, C.; Dong, J. S.; Schnablegger, H.; Katsoulakis, M. A.; Kokkoli, E.; McCormick, A. V.; Penn, R. L.; Tsapatsis, M. *Nat. Mater.* **2006**, *5*, 400.
- (30) Li, Q. H.; Mihailova, B.; Creaser, D.; Sterte, J. *Microporous Mesoporous Mater.* **2001**, *43*, 51.
- (31) Corma, A.; Martinez-Triguero, J.; Martinez, C. *J. Catal.* **2001**, *197*, 151.